Towards Reliable Li-metal-free LiNO3-free Li-ion Polysulphide Full Cell via Parallel Interface Engineering

Journal:	*Energy & Environmental Science*
Manuscript ID	EE-ART-03-2018-000937.R2
Article Type:	Paper
Date Submitted by the Author:	14-Jun-2018

Complete List of Authors:	Sun, Ju; University of New South Wales, School of Chemical Engineering Liang, Jiaxing; University of New South Wales, School of Chemical Engineering Liu, Junnan; University of New South Wales Shi, Wenyan; University of New South Wales, School of Chemical Engineering Sharma, Neeraj; UNSW Australia, Chemistry; Lv, Wei; Tsinghua University, Graduate School at Shenzhen Lv, Ruitao; Tsinghua University, Yang, Q. H.; Tianjin University, Amal, Rose; The University of New South Wales, School of Chemical Sciences and Engineering Wang, Dawei; University of New South Wales, School of Chemical Engineering

SCHOLARONE™
Manuscripts

Towards Reliable Li-metal-free $LiNO_3$-free Li-ion Polysulphide Full Cell via Parallel Interface Engineering

Ju Sun[a], Jiaxing Liang[a], Junnan Liu[b], Wenyan Shi[a], Neeraj Sharma[b], Wei Lv[c], Ruitao Lv[d, e], Quan-Hong Yang[f], Rose Amal[a], Da-Wei Wang[a*]

[a] *Particles and Catalysis Research Group, School of Chemical Engineering, The University of New South Wales, Sydney, NSW 2052, Australia*

[b] *School of Chemistry, The University of New South Wales, Sydney, NSW 2052, Australia*

[c] *Shenzhen Key Laboratory for Graphene-based materials and Engineering Laboratory for Functionalized Carbon Materials, Graduate School at Shenzhen, Tsinghua University, Shenzhen, 518055, China*

[d] *State Key Laboratory of New Ceramics and Fine Processing, School of Materials Science and Engineering, Tsinghua University, Beijing 100084, China*

[e] *Key Laboratory of Advanced Materials (MOE), School of Materials Science and Engineering, Tsinghua University, Beijing 100084, China*

[f] *Key Laboratory for Green Chemical Technology of Ministry of Education, School of Chemical Engineering and Technology, Tianjin University, Tianjin, 300072, China*

Corresponding author. Tel.: +61-2-9385-7355; e-mail: da-wei.wang@unsw.edu.au

Abstract

There has been intensive concentration and effort on addressing the notorious challenges of Li-S batteries with respect to the polysulphide utilization and the lithium dendrite inhibition. However, the search and optimisation of the Li-metal-free full cell design remain relatively pre-mature in terms of the generic synchronous approach to improve the anode/cathode stability while balancing the anode/cathode capacity. We hereby report a parallel interface engineering (PIE) strategy to enhance the full-cell performance of the Li-ion polysulphide battery. Very importantly, this PIE strategy allows the use of Li-metal-free anode and the $LiNO_3$-free electrolyte. The cell-level improvement is attributable to the more efficient and uniform lithium sulphides deposition on the chemically uniform surfaces of the carbon cathode and the suppressed growth of dendritic species on the Li-Al alloy anode with an implantable solid-electrolyte interphase. The quantitative electrochemical alloying for anode fabrication allows the increased lithium utilization relative to the total anode capacity. The PIE strategy represents a facile approach to address the troublesome issues of Li-S batteries at the full cell level.

Keywords

Lithium-sulphur batteries; full cell; lithium alloy; polysulphide; carbon electrode

Introduction

In recent years Li-S battery becomes a promising beyond-Li-ion candidate in the future energy storage sector on account of many advantages: low cost, high theoretical capacity of sulphur (1675 mA h g^{-1}), and higher energy density 2500 Wh kg^{-1}. Nevertheless, the most notorious challenges to date that hinder its commercialization remains unsolved. A typical Li-S full cell utilizes a sulphur/carbon cathode and a lithium metal anode. The high solubility of polysulphides usually results in the capacity decay during cycling because of the deposition of migrating polysulphides in forms of insoluble species at the anode[1]. This condition occurs along with the growth of Li dendrites, which could impair the cell stability and safety. To date, despite the emerging materials innovations on the promoted sulphur-based cathodes or the stabilized lithium metal anodes, the search of new configurations and strategies for full cell design is in the infancy[2–4]. A harmonic design of the full cell should essentially consider the balance of the reversible total capacity of the cathode and the anode, and more critically deal with synchronously the stabilization and utilization of sulphur/polysulphide on cathode and the dendrite inhibition and surface passivation of the anode.

The design of conductive nanoscale network as sulphur host has been a major strategy that could combine both 'sulfiphilic' chemical affinity and physical confinement to collectively stabilize sulphur/polysulphide species. The physical accommodation of sulphur within micro-/meso-porous carbon mateirlas[5,6] could effectively confine polysulphides, as well as supress the volume expansion. Meanwhile, the 'electrocatalytic' effects of chemical capture and conversion of polysulphide is widely investigated by introducing heterogeneous carbons containing nitrogen, oxygen, sulphur, or phosphorus[7–10], and semi-conductive/metallic polar chemicals (metal sulphides/carbides/nitrides/oxides, polymers, etc[11–15]). Carbon-based current collectors are deployed for semi-liquid Li-polysulphide batteries[16–18]. Nonetheless, the deposition and growth of Li_2S on carbon, and the impact of the precipitation morphology on the interface charge transfer, are poorly understood. Since the sulphide deposition forms an insulating layer on the surface of cathode, it is critical to maintain the layer as thin as possible to modulate the charge transfer resistance in a kinetically favourable region. Otherwise, the thick passivation precipitation would impair the charge transfer between the electrolyte and the conductive interface[19–21]. In this work, we demonstrate the improved kinetics and sulphur utilization efficiency of the uniform Li_2S deposits-on tailored carbon surfaces with chemical homogeneity.

On the other side, in spite of its large capacity, the applicability of Li metal has been challenged by the dendrite growth, the instable interphase, and the irreversible reaction with polysulphide. Thick lithium foil (50–100 mA h cm^{-2} areal capacity) is often used in Li-S half-cell along with anode surface stabilizer (such as $LiNO_3$)[22,23]. However, this configuration is unlikely feasible for full cell operation because of the low lithium utilization efficiency (<5 %) and the irreversible supply of $LiNO_3$ to repair the repetitive interphase breakdown during long cycles. Recently, lithium alloy anodes have received increasing attention on account of their high theoretical capacity (e.g., Li_9Al_4: 2980 mA h g^{-1}; $Li_{22}Si_5$: 4200 mA h g^{-1}; $Li_{4.4}Sn$: 990 mA h g^{-1})[24]. Lithium-containing alloy has been used as Li-metal-free anode to couple with sulphur cathode for Li-ion-S full cells[25,26]. The advantages of employing Al-Li alloy anode was discussed previously[27], which include the least volume change of Al-Li alloy among many others (Al: 96 %, Si: 320 %, Sn: 260 % and Sb: 200%), high gravimetric and volumetric capacity (2980 mA h g^{-1} and 8046 mA h cm^{-3}), and moderately positive potential (0.2 – 0.3 V vs. Li^0/Li^+) to lithium metal. However, the inhibitive effects of the alloy anode on the dendrite growth and polysulphide reduction (especially in the absence of anode surface stabilizers, such as $LiNO_3$) are rarely studied. New insight into the interface stability of lithium alloy anode in Li-ion-S full cell is indicative for the design of reliable full cells. In this work, we demonstrate the feasibility of using an electrochemically fabricated Al-Li alloy anode with an implantable solid-electrolyte interphase (SEI) to stabilize the dendrite growth and to retard the polysulphide consumption in a $LiNO_3$-free Li-ion-polysulfide full cell.

As such, we propose a parallel interface engineering (PIE) strategy to design a reliable Li-ion-polysulphide full cell. This PIE strategy deploys the electrochemical alloying method to make Al-Li alloy, which not only increases the Li use efficiency but also produces the implantable SEI on the alloy anode that allows the use of $LiNO_3$-free electrolytes. On the other side, this PIE strategy uses carbon host with chemically homogeneous surface to load the $LiNO_3$-free polysulphide catholyte with pre-determined anode-matching capacity. As a consequence, a Li-metal-free $LiNO_3$-free Li-ion-polysulphide full cell with matched anode and cathode capacity, as well as tailored electrode architecture and composition, is achieved. Our results show that the interface stability of the Al-Li alloy anode is largely strengthened in comparison with Li metal. At the meantime, the more uniform surface chemical environment at the hydrothermally modified carbon cloth was found to facilitate the homogeneous deposition of Li_2S films with improved charge transfer kinetics. In the absence of $LiNO_3$, this Li-ion-

polysulphide full cell exhibited a high gravimetric capacity of 1,050 mA h g^{-1} at 0.2 C (based on the sulphur mass), and preserved 500 mA h g^{-1} capacity with nearly 100 % coulombic efficiency at the 100^{th} cycle.

Experimental methods

Hydrothermal surface coating of carbon cloth

All the materials were used as received. Carbon cloth (supplied by Activated Charcoal) was firstly washed by 2 M HCl through sonication for 5 times and deionized water for 2 times in order to remove any impurities. Then the carbon cloth was dried at 80 °C to remove water for 12 h. 2.5 g D-glucose (Sigma Aldrich) and 12.5 mg sodium dodecyl sulphate (SDS, Sigma Aldrich) was dissolved into 50 mL water together with carbon cloth by ultrasonication to get homogenous solution. Then the solution was transferred to a 100 mL Teflon autoclave and heat at 190 °C for 15 h. The dark brown sample was taken out after hydrothermal reaction and washed with deionized water for 5 times and dried at 80 °C overnight. This was then calcined at 800 °C under N_2 atmosphere for 4 h to produce the hydrothemal carbon@carbon cloth (HTC-CC) products. The washed carbon cloth (CC) was also calcined under the same condition before battery assembly. Both CC and HTC-CC were punched into small disks with diameters of 8 mm (~0.5 cm^2), and the mass was 8 mg and 10 mg respectively. The glucose-derived hydrothermal carbon coating accounted for approximately 20% of the total weight of HTC-CC.

Preparation of Al-Li alloy

The Al-Li alloy was prepared via an electrochemical method. Briefly, CR2032-type coin cells with lithium foil as an anode and aluminium foil (15 μm) as a cathode were assembled. A 1M $LiPF_6$ in ethylene carbonate/ethyl methyl carbonate (EC/EMC, v/v=1:1) was used as electrolyte and a Celgard 2500 polypropylene membrane was used as a separator. After discharge, the coin cell was disassembled and the Al-Li alloy was recovered, washing by dimethyl carbonate (DMC) to remove any residues.

Preparation of electrolyte and catholyte for Li-ion-polysulfide full cell

The blank electrolyte was prepared by dissolving an appropriate amount of Bis(trifluoromethane)sulfonimide lithium salt (LiTFSI, 99.95%, Sigma Aldrich) in Triethylene glycol dimethyl ether (TEGDME, 99%, Sigma Aldrich). In order to prepare lithium polysulphides solution, a certain amount of lithium sulphide (Li_2S, 99.98%, Sigma

Aldrich) and sublimed sulphur (Sigma Aldrich) were mixed in TEGDME solution and stirred at 60 °C overnight. Finally, 1 M brown-red Li_2S_4 catholyte was fabricated. The molarities were based on the sulphur amount. All procedures were done inside an Ar-filled glove box. *$LiNO_3$ was not used in any case*.

Electrochemical measurement of full cell

The Al-Li | HTC-CC full cell was assembled in the glove box. First of all, 12 μL of 1 M Li_2S_4 was loaded onto the HTC-CC current collector. Then a Celgard 2500 polypropylene membrane was used as the separator, followed by a drop of 20 μL blank electrolyte on the separator. At last, Al-Li alloy was placed on the separator. A control test with CC current collector was assembled with the same procedure. Galvanostatic charge-discharge cycles were carried out using a Land battery tester (CT2001A). The cyclic voltammetry and electrochemical impedance spectroscopy were conducted using a Biologic VSP potentiostat.

Assessing anode stability in polysulphide

Both fresh Li metal and as-prepared Al-Li alloy were soaked into Li_2S_4 solution. The concentration of Li_2S_4 was 2 M. After 48 h, the samples were washed with TEGDME solvent three times and dried under vacuum overnight for further tests.

In-situ X-ray diffraction studies

Half cells with 3 mm diameter holes in the casing and 5 mm diameter holes in the stainless spacer were used for the construction of the coin cells for the *in situ* XRD measurements. The CR2032 coin cells were constructed in an Ar-filled glove box and contained the same assembly as mentioned in the preparation of the Li-Al above. *In situ* synchrotron XRD experiments were performed 3-4 days after cell construction. Further details regarding coin cell construction and beamline setup can be found in our previous publications[28,29].

In situ synchrotron XRD data were collected on the Powder Diffraction beamline at the Australian Synchrotron with wavelengths determined by refining a structural model with data collected on a NIST 660b LaB_6 standard reference material. Data was collected at 0.708735 Å for a period of 3.2 minutes in intervals of 28 minutes during discharge.

Characterization

The morphology of Al-Li alloy and Li metal were obtained by scanning electron microscopy (SEM) via a FEI Nova NanoSEM 450 FE-SEM microscope at an accelerating voltage of 5

kV. The elemental mapping results were examined through an energy dispersive spectrometer (EDS) attached to the FEI Nova NanoSEM 450 FE-SEM. XRD pattern of the Al-Li alloy was collected on a PANalytical Empyrean II diffractometer with Cu Kα radiation (λ = 0.15406 nm) at 45 kV and 40 mA. The sample was placed in an air-sensitive sample holder in the Ar-filled glove box prior to data collection. The X-ray photoelectron spectroscopy (XPS) was performed on a Thermo Scientific, UK (model ESCALAB250Xi) using Mg Kα (hν = 1486.68 eV) as the excitation source with 150 W power (13 kV x 12 mA). For all of the cycled samples, including Al-Li alloy, HTC-CC and CC current collector, they were first recovered from coin cells in the glove box, washed by TEGDME solvent three times, and dried under vacuum overnight. Then the samples were sealed and transported for these *ex-situ* tests (XRD, XPS, SEM).

Results and discussion

Cathodic lithium sulphides deposition on carbon surface

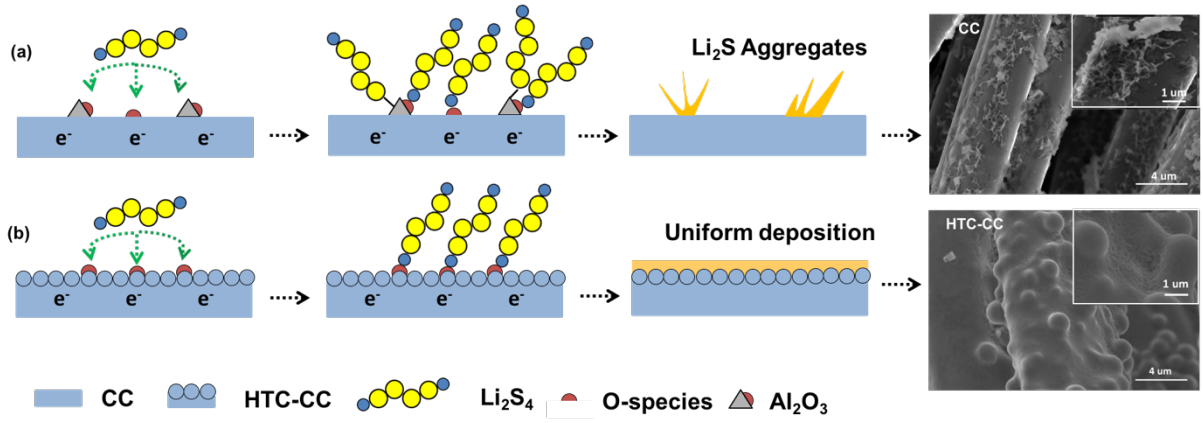

Fig. 1 The effect of surface chemistry on the Li_2S precipitation. (a) the Al_2O_3-containing contaminated surfaces of the commercially purchased CC provide "sulfiphilic" sites for the preferential deposition of Li_2S through polar-polar interactions. (b) the hydrothermally modified HTC-CC with uniform carbon surfaces containing oxygen functional groups is prone to plate uniform Li_2S film. The SEM images show the morphology of the Li_2S deposits on CC and HTC-CC surfaces after full discharge; inset is the corresponding high-magnification image.

Carbon cloth was adopted as the substrate to investigate the effect of the carbon surfaces on the lithium sulphides deposition. We used commercially available carbon cloth (CC)

as the cathode matrix after successive acid leaching and calcination. The interwoven fibre structure of the CC is shown in Fig. S1a. The diameter of the CC fibres is between 4 and 6 μm. We further hydrothermally treated the acid-leached CC in a vessel containing an aqueous glucose solution. As shown in Fig. S1b and S2, the surface of the treated CC is modified with hydrothermal carbon (HTC-CC) consisting of both spherical particles and film coating on the fibres, as evidenced by the uniform surface in Fig. S1b and the surface chemical analysis (to be discussed later). The evolution of the porosity before and after the hydrothermal treatment was probed by using the N_2 adsorption-desorption as displayed in Fig. S3. The population of micropores for HTC-CC is remarkably reduced in comparison with that of CC[30]. The Brunauer-Emmett-Teller (BET) surface area for HTC-CC dropped to 686 $m^2 g^{-1}$ with respect to the 1445 $m^2 g^{-1}$ of CC. By applying the CC and HTC-CC as the cathode substrate for lithium polysulphide (Li_2S_4), the morphology of the discharged lithium sulphides deposition was investigated using scanning electron microscopy (SEM). The SEM images in Fig. 1a reveal the uneven whisker-like agglomerates on the surface of the CC fibres. In stark contrast, Fig. 1b displays the uniform feature-less film-like lithium sulphides deposits, which is homogeneously distributed on the surfaces of the HTC-CC fibres. Such uniform lithium sulphides deposition on HTC-CC is likely thinner than the whisker-like agglomerates on CC, and could be beneficial for fast charge transfer (according to the impedance measurement discussed later). Recently, Pan et al.[19] suggested the key role of carbon surface chemistry in governing the lithium sulphides deposition. The significant morphological difference of the Li_2S deposition between HTC-CC and CC is thus reasonably attributable to their distinct surface properties.

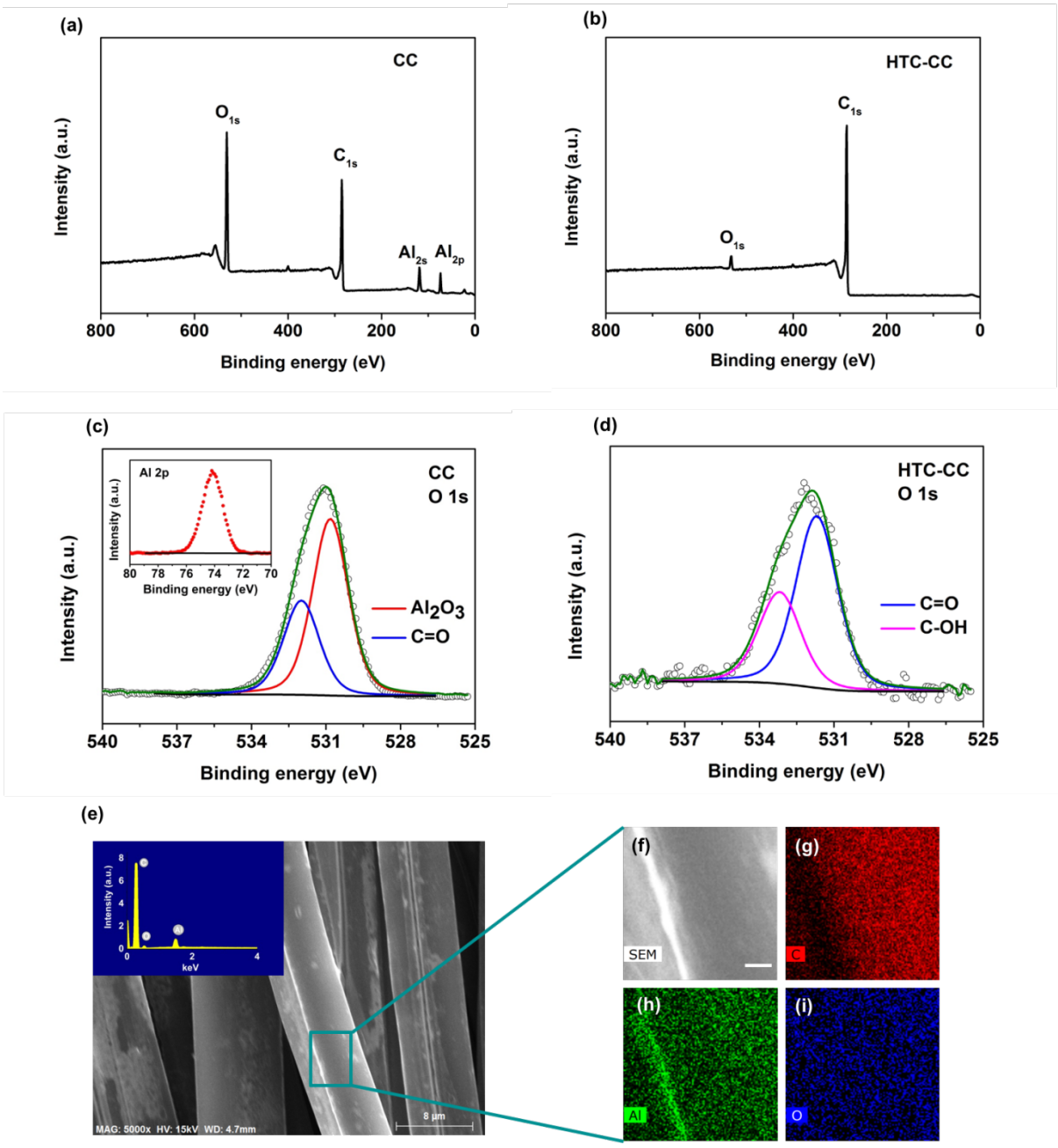

Fig. 2 XPS full spectra of (a) CC and (b) HTC-CC. XPS O 1s spectra for (c) CC and (d) HTC-CC. The inset picture in (c) is the Al 2p of CC. (e) SEM images of CC, inset is the EDS spectrum. EDS element mapping of the CC surface (f) secondary electron image, (g) carbon, (h) aluminium, and (i) oxygen, the scale bar in (f) is 1 μm.

The XPS full spectra of CC and HTC-CC in Fig. 2 (a, b) show the existence of C, O as the primary constitutions. A strong signal of Al was also observed on the surface of CC. Considering the fact that the CC is a commercial product and was only purified by acid leaching, the Al species are likely Al_2O_3 contaminations. In comparison, the surface of HTC-

CC is rather pure containing only carbon and oxygen elements. Fig. 2c and d show the deconvoluted XPS O 1s spectra of CC and HTC-CC. The two samples exhibit a typical peak of C=O functional groups at around 531.7 eV (CC) and 531.9 eV (HTC-CC), respectively; while HTC-CC sample has a peak of C–OH functional groups at 533.2 eV. The O 1s peak in CC at 530.8 eV corresponds with Al_2O_3 (Fig. 2c)[31]. The spatial distribution of Al_2O_3 on CC fibres was tracked by using EDS mapping. As shown in Fig. 2 (f-i), there are strong Al signals spreading throughout the whole fibre surface. Al_2O_3 was reported to be a good absorbent to polysulphides compared with many metal oxides (such as CeO_2, MgO, CaO, etc.)[15]. The Al^{3+} centre of Al_2O_3 is Lewis acid while polysulphides are Lewis base. Therefore, the Al^{3+} is intrinsically a "sulfiphilic" site to interact with polysulphide during the discharge process. Meanwhile, the O^{2-} centre of Al_2O_3 is affinitive to Li^+ cations, facilitating the Li^+ mediated capture of polysulphides[32]. During the discharge process, the strong interaction of lithium polysulphides (Li_2S_n) with the Al_2O_3 sites could give rise to the facilitated nucleation and growth kinetics, in comparison with the less affinitive Al_2O_3-free surface of HTC-CC. As depicted in Fig. 1a, this could lead to the non-uniform deposition of Li_2S due to the spatially different interactions of polysulphides with carbon and Al_2O_3 sites. Because of this site-specific uneven nucleation distribution, the growth of agglomerated Li_2S particles on CC is relatively hard to prohibit. The Li_2S aggregation could eventually lead to the large interfacial resistance as discussed later. In contrast, the hydrothermal treatment produces a uniform carbon coating on the bare CC substrate, resulting in a rather clean surface of HTC-CC. The HTC covering contains only carbon and oxygen and conceals the contaminating Al_2O_3 which are un-detectable with XPS. The polysulphides are thus isolated from the Al_2O_3 species and solely interact with the carbon/oxygen species on HTC-CC surface. Therefore, the mild carbon/oxygen-polysulphide interaction at the HTC-CC is beneficial to the formation of more electro-active sulphide deposition, in comparison with the strong Al_2O_3-polysulfide interaction[19]. Further control experiment was carried out to validate the correlation of the Li_2S morphology with the surface property of carbon cloth. An Al_2O_3-free Kynol CC sample was used as the cathode to precipitate Li_2S (Fig. S4). SEM analysis revealed the uniform coverage of small particles with comparable dimensions on the surface of the Al_2O_3-free Kynol CC cathode (Fig. S5). This phenomenon is intrinsically unlike the selective spatial distribution of Li_2S on the Al_2O_3-exposed CC, yet is comparable with the HTC-CC in regards of the uniform spatial distribution and small particle size. The tailored substrate-polysulphide interaction is thus suggested responsible for the different electrochemical behaviour of polysulphide on HTC-CC and CC cathodes.

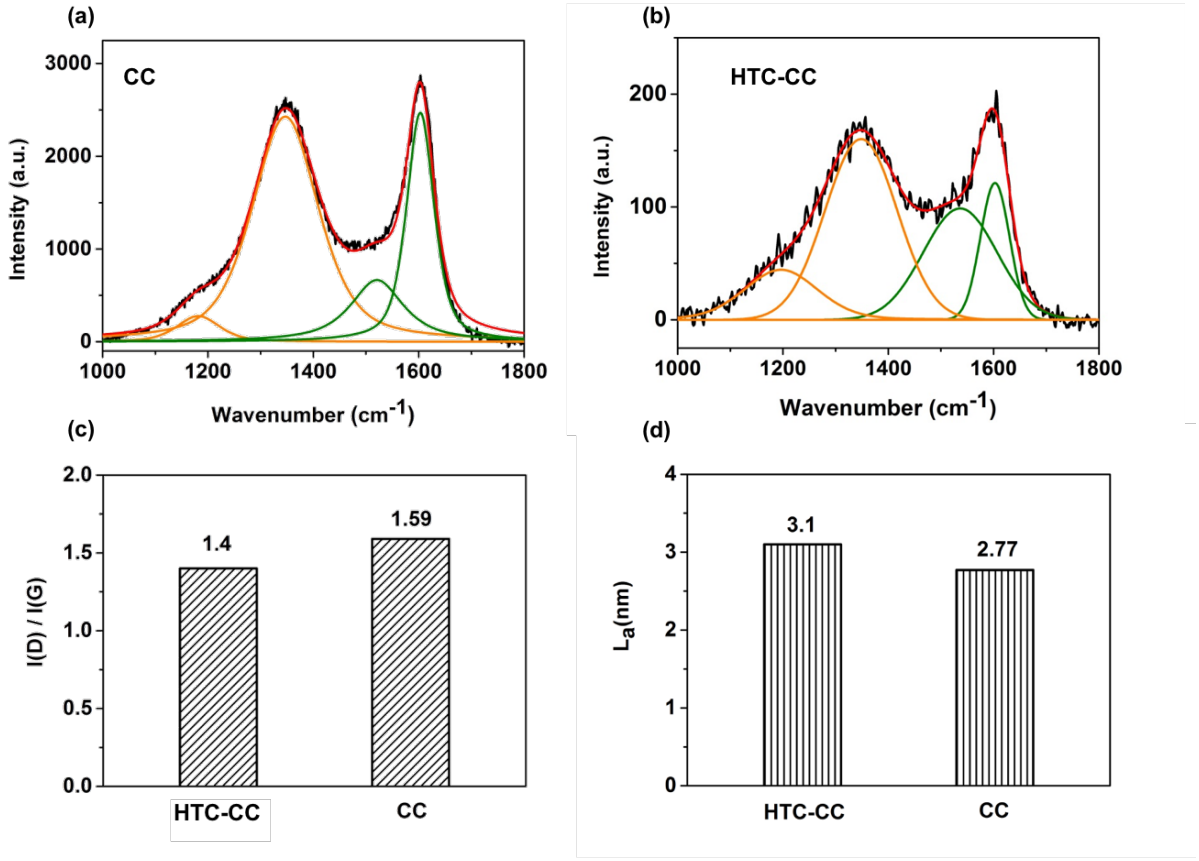

Fig 3. Raman spectroscopic analysis of CC and HTC-CC polysulphide reservoirs. Raman spectra for (a) CC and (b) HTC-CC; (c) I(D)/I(G) for CC and HTC-CC; (d) Lateral graphite micro-crystal size for CC and HTC-CC.

The graphitic structure of carbon will also affect the electrode kinetics. Raman spectroscopy was employed to characterise the graphitic feature of CC and HTC-CC. Fig. S6 displays the two typical peaks at 1350 cm^{-1} (D band) and 1600 cm^{-1} (G band) obtained from CC and HTC-CC. The deconvoluted Raman profiles are shown in Fig. 3 (a, b). These peaks are fitted using Gaussian mode with two prominent peaks centred at 1350 cm^{-1} and 1600 cm^{-1}, and two broad peaks at 1180 cm^{-1} and 1520 cm^{-1}, where the two broad peaks (1180 cm^{-1} and 1520 cm^{-1}) were attributed to amorphous carbon structures[33]. The G band at 1600 cm^{-1} is characteristic of the graphitic structure, while D band at 1350 cm^{-1} is the signal of disordered carbon. The HTC-CC sample has narrower bandwidth than that of CC, showing the higher degree of graphitic structure[34,35]. Fig. 3c compares the ratio of I(D)/I(G) for CC and HTC-CC samples. HTC-CC has lower value (1.4) than that of CC (1.59), indicating the lower degree of amorphous structure. Tuinstra and Koenig et al[35] reported the ratio of I(D)/I(G) varied inversely to L_a,

$$\frac{I(D)}{I(G)} = \frac{C(\lambda)}{L_a} \qquad (1)$$

where C (λ) is around 44 Å, corresponding with the 514.5 nm laser; L_a is the cluster dimension or in-plane correlation length; I(D) and I(G) are the area of D and G bands, respectively. The corresponding calculation of carbon(sp^2) microcrystal size is compared in Fig. 3d. The planar microcrystalline size of HTC-CC (3.1 nm) is larger than that of CC (2.77 nm), indicating the surface of HTC-CC is less defective[33]. The improved crystallinity of HTC-CC in comparison with CC improves the electron transport due to the reduced scattering defective sites. At the meantime, the reduced density of defects in the carbon also homogenise the nucleation sites for lithium polysulphides.

Interface stability of alloy anode with implanted SEI

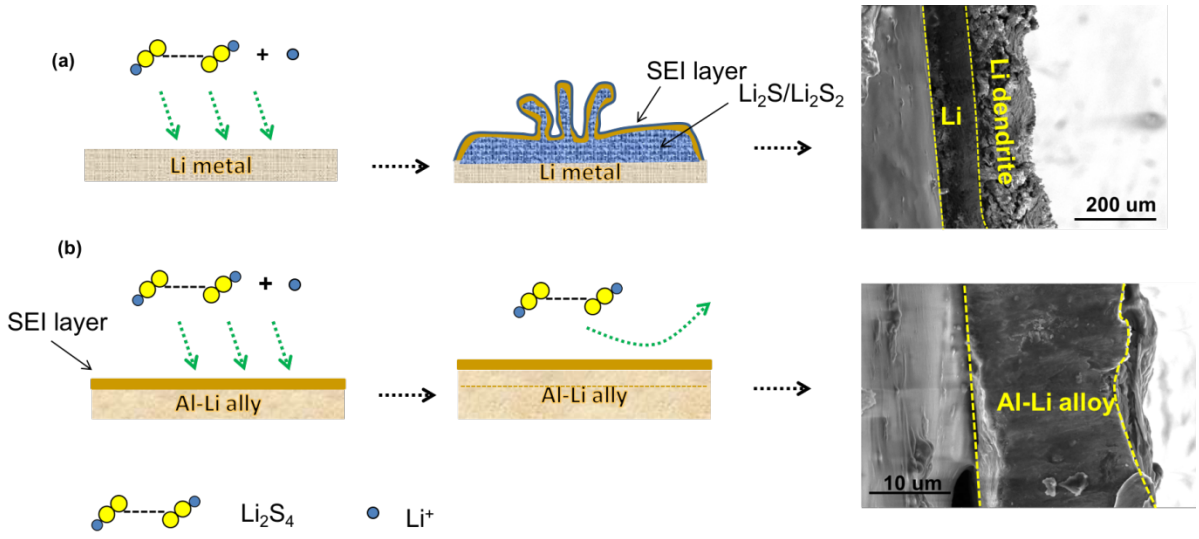

Fig. 4 The interface stability of Al-Li alloy and Li metal in polysulphide solution. (a) Illustration of the formation of SEI layer and lithium dendrite at the surface of bare Li metal after exposure in lithium polysulphide solution. The SEM image shows the porous cross-section of the immersed lithium metal foil. (b) Illustration of the stabilized interface of Al-Li alloy in lithium polysulphide solution. The interface stability is attributed to the protection by the implantable SEI layer formed during the electrochemical alloying. The SEM image shows the dense cross-section of the immersed Al-Li alloy foil.

The interface stability of Li metal and Al-Li alloy in a $LiNO_3$-free polysulphide solution was compared, as illustrated in Fig. 4. The comparison of the interface reactivity of lithium metal and Al-Li alloy without anode surface stabilizer could reflect their respective suitability for full cell configuration. A 200 μm thick Li metal (its original cross-section is shown in Fig.

S7a) was directly immersed into a lithium polysulphide solution for 48 h. The cross-sectional SEM images in Fig. 4a revealed the dendrite growth and the coarse exterior which were resulted from the high reactivity of lithium in polysulphide catholyte without appropriate surface protection (i.e. $LiNO_3$ assisted surface passivation)[22,23]. On the other hand, we used an electrochemical alloying method to prepare the Al-Li alloy in carbonate electrolyte (EC/EMC, v/v=1/1) from a 20 μm thick Al foil. The cross-section of the original Al-Li alloy is shown in Fig. S7b. The alloying process created the SEI layer on top of the alloy layer, as illustrated in Fig. 4b. As a result, the surface and exterior structures for the soaked Al-Li alloy preserved the nearly identical morphology without the formation of voids or flakes, indicating the superior interface stability. Capacity matching between anode and cathode was also investigated (calculation in Supporting Information). The anode capacity is 2.6 times of the cathode with more than 50% lithium utilization. While in most of Li-S half cells, the utilization of lithium metal anode is less than 10 % (Supporting Information), which more or less alleviates the dendrite problems. However, with pouch-type Li-S full cell, the lithium anode deteriorates rapidly as a result of the dendrite growth at higher lithium utilization[36].

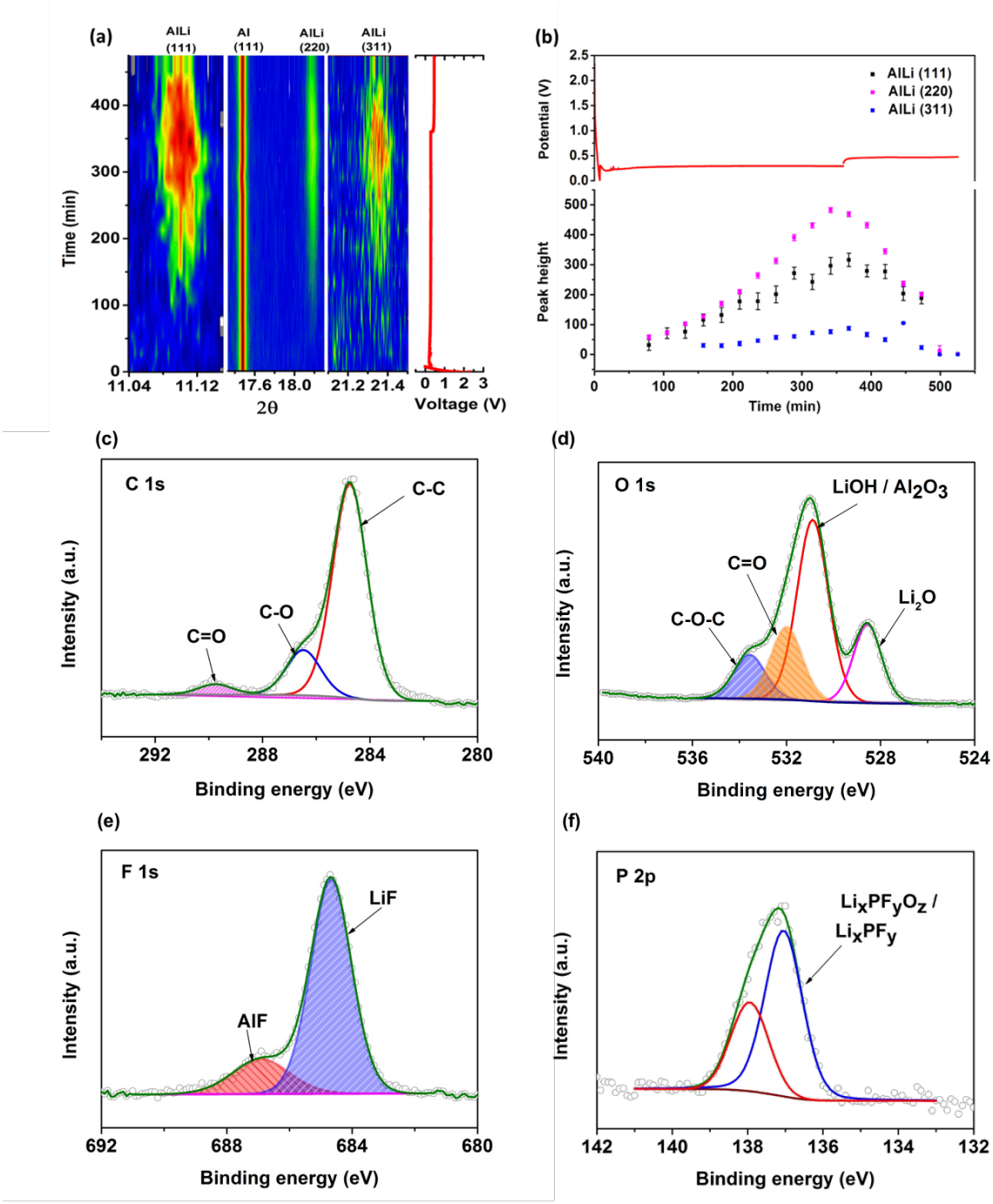

Fig. 5 (a) The contour plot of XRD patterns (left) and voltage profile (right) of Al-Li alloying at 0.01 mA cm^{-2}; (b) peak fitting parameters of three peaks corresponding with the Al-Li alloy phase; (c-f) XPS spectra of C 1s, O 1s, F 1s and P 2p on the surface of Al-Li alloy.

The phase transition and surface composition of Al-Li alloy anode were investigated to understand its behaviour as a substitute to Li metal anode. Al-Li alloy anode was electrochemically prepared in a half cell, which is shown in Fig. S8 with alloying potential at 0.3 V and de-alloying potential at 0.42 V. The *in-situ* half cell employed a Kapton-sealed

window for XRD analysis. The contour plot in Fig. 5a indicates a typical alloying process. These reflections at 2θ = 11.10°, 18.9° and 21.36° at λ = 0.708735 Å can be indexed as AlLi (111), AlLi (220) and AlLi (311), respectively. Another additional strong reflection at a constant position at 2θ = 17.45° is from Al foil at the anode. The peak fitting in Fig. 5b revealed the volcano-shaped trend of the peak height for all three AlLi peaks, which corresponds to the alloying and the de-alloying of lithium. The high-resolution XPS spectra of C 1s, O 1s, F 1s and P 2p shown in Fig. 5 (c-f) elaborate the surface compositions of Al-Li alloy. The C 1s spectra in Fig. 5c showed a dominant peak centered at 284.5 eV corresponding to the sp^2 C–C bond, which was consistent with the electrolyte decomposition residues. The additional peaks at 286.5 eV and 289.8 eV were correlated with lithium alkyl carbonate species, where both CH_2–O, and O–(C=O)–O were recognised. The peaks at 533.6 eV and 532 eV in O 1s as shown in Fig. 5d were in good agreement with C 1s spectra and confirmed the existence of Li_2CO_3[37]. The peaks at 528.6 eV and 530.9 eV are attributable to Li_2O and LiOH species. Both species are derived from the electrolyte decomposition. The F 1s profile in Fig. 5e demonstrates the LiF and AlF species that were derived from the side reaction of Li_2CO_3 and aluminium species with PF_6^-[38]. The other salt reduction products of Li_xPF_y and $Li_xPF_yO_z$ in Fig. 5f were identified as the composition of solid electrolyte interphase (SEI)[39,40], where the Li_xPF_y could be oxidized to $Li_xPF_yO_z$ when exposed to air[40]. The main composition of precast SEI on the alloy lies in the LiF, which was reported to effectively stabilize the SEI layer through fast Li-ion diffusion, and could enable smooth Li platting/stripping[41–43]. The SEI component for the Al-Li alloy anode after cycling in TEGDME solvent of the full cell was analysed and compared with the SEI layer on the as-prepared alloy (Fig. S9). In the C 1s spectra, the SEI formation on the as-prepared Al-Li alloy in $LiPF_6$+EC/EMC has the similar component with the one cycled in TEGDME solvent, which is derived from the electrolyte decomposition, like CH_2–O, and O–(C=O)–O. In the O 1s spectra, both alloy anodes contain Li_2O and LiOH species in spite of the different solvents, which are consistent with the Li 1s spectra. While for the cycled sample, the signal of Li_2CO_3 component was not detected, which could be attributed to the change of solvent (from carbonate to ether electrolyte). There is a sharp peak of $–CF_3$ in the F 1s spectrum of the cycled alloy sample, which is the decomposition product of LiTFSI salt during cycling. The LiF species in F 1s spectra dominate the surface chemistry of original SEI layer, and further stabilize in the new SEI formed during cycling.

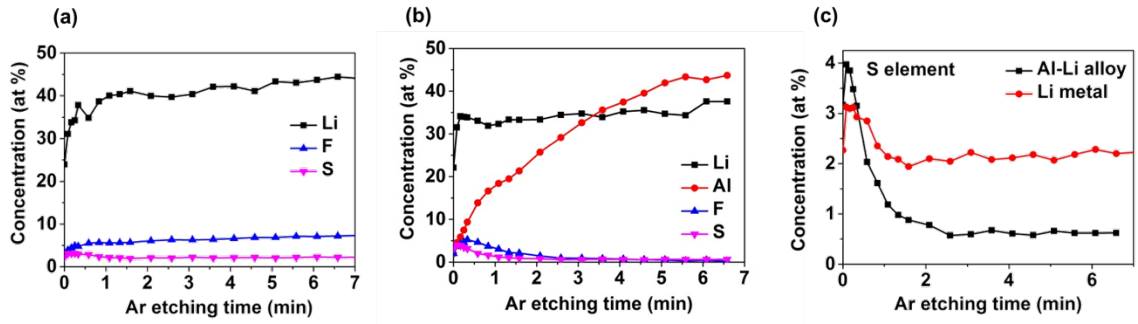

Fig. 6. The XPS elemental depth profile of Li metal (a) and Al-Li alloy (b) after soaking in the catholyte. (c) The comparison of the sulphur content depth profile for Li metal and Al-Li alloy

Since the Al-Li alloy was prepared within carbonate electrolyte (EC/EMC, v/v=1/1), it is necessary to know whether SEI on the surface of alloy could be compatible with ether electrolyte (TEGDME). Fig. S10 shows the HOMO/LUMO of both SEI composition and electrolyte solvent, and the gap energy was calculated at B3LYP/6-31G, (2df, p)[44]. According to Cheng et al.[45], when the highest occupied molecular orbital (HOMO) of solvent is lower than the lowest unoccupied molecular orbital (LUMO) of SEI, and the LUMO of solvent is higher than the HOMO of SEI, the SEI is thermodynamically stable in the ether electrolyte. Fig. S11 recorded the XPS spectra of both Al-Li alloy and Li metal after LiPS soaking test. The increased signal of C–C peak in Fig. S11a along with Li_2CO_3 species in Fig. S11b both show the stable SEI layer on Al-Li alloy when compared with Li metal. The strong peak of LiF is the main component of SEI, and can effectively protect the surface of anode from polysulphides. The additional $–CF_3$ peak is derived from the decomposition of LiTFSI in TEGDME electrolyte. The elemental depth profiles of Li, F, S, and Al were recorded to derive the spatial formation of the lithium sulphide deposition and the SEI, as shown in Fig. 6 (a, b). With the Ar etching time increases, the sulphur content in the lithium metal reduces, while the fluorine amount increases, according to Fig. 6a. This trend shows the lithium sulphide deposition mainly resides in the sub-surface region, while the SEI penetrates relatively deeply into the bulk of the lithium metal. The bare Li metal reacts actively with the electrolyte that induces the SEI formation and polysulfide consumption, and cause structural cracks as a result of the phase change, volume expansion, and void formation. These are in agreement with the dendritic and coarse structure of the soaked lithium metal. In contrast, the concentration of both sulphur and fluorine on the soaked Al-Li alloy reduces quickly within a 2-min Ar etching period, demonstrating the much shallower distribution of lithium sulphides and SEI . Furthermore, the concentration of sulphur in the lithium metal is nearly 4 times of

that in the Al-Li alloy (Fig. 6c), suggesting the largely suppressed irreversible deposition of polysulphide on the surfaces of the Al-Li alloy. The above results revealed the advantageous nature of utilizing the Al-Li alloy as an anode in full cell for Li-S batteries, for the sake of the reduced dendritic morphology and sulphur cost.

The suppression of the polysulfide reaction on the Al-Li alloy might be due to 1) the Al-Li alloy was protected by a precast and implantable SEI layer during the alloy synthesis that consists of both inorganic and organic electron-isolating components that should minimize the electron transfer between the alloy and the polysulfide or electrolyte, and 2) the Li atoms in the Al-Li alloy bind strongly with the surrounding Al atoms, which are able to stabilize the reactive lithium atoms upon exposure to the electrolyte or lithium polysulphides. While many mechanisms are plausible for the dendrite inhibition, it is worth noting that as the Al potential is limited above the Li/Li^+ potential by 0.3 V, the lithium metal deposition is thermodynamically unfavourable. On the other side, the alloying requires the inward diffusion of lithium atoms into the bulk of the Al foil to form the alloy binding, rather than the outward plating of lithium from the top surface of the Al foil. Compared with the outward/epitaxial deposition of lithium on lithiophilic carbons that has a very low alloying potential (0.01 V) above Li/Li^+, the alloying process with Al can intrinsically prevent the growth of dendrite due to the effective interface confinement caused by electrode kinetics and mass transport.

Li-ion polysulphide full cell

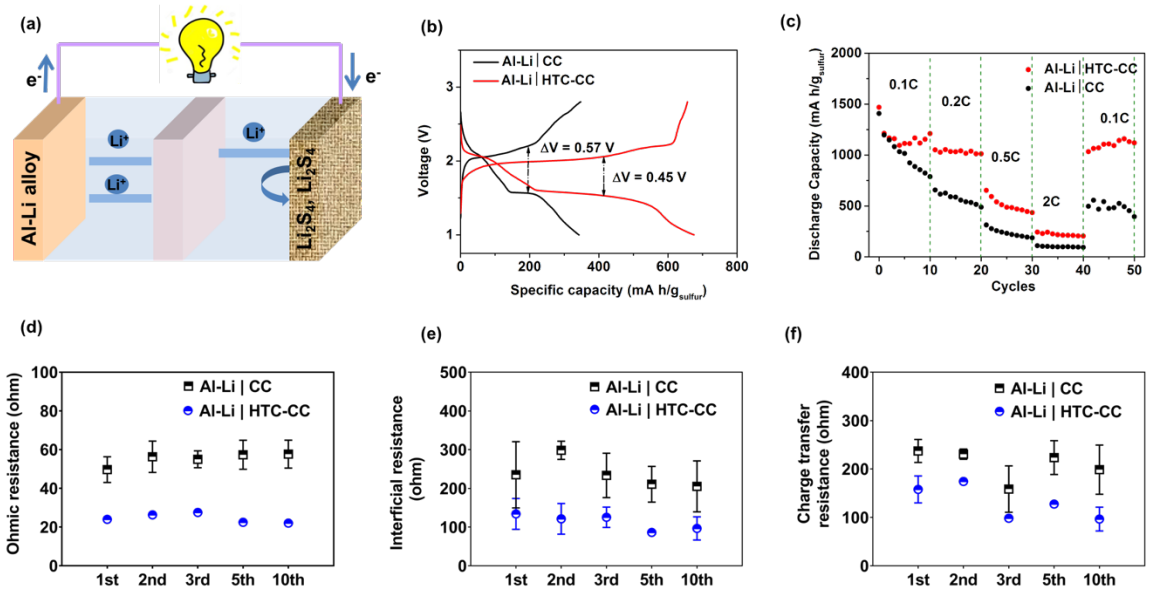

Fig. 7 (a) Full cell schematic with Al-Li alloy as anode and HTC-CC as polysulphide current collector; (b) 10^{th} cycle charge and discharge curve and (c) rate performance of Al-Li | CC and Al-Li | HTC-CC full cell (current density is 0.2 C, 1 C=1675 mA g^{-1}); (d-f) EIS measurement of Al-Li | CC and Al-Li | HTC-CC full cell after 1^{st}, 2^{nd}, 3^{rd}, 5^{th} and 10^{th} cycle of discharge state at 0.1 C ; namely Ohmic resistance (d), charge transfer resistance (e) and interfacial resistance (f). The EIS tests were replicated three times. Note that $LiNO_3$ was not added in either case.

Fig. 7a shows a full cell design with Al-Li alloy as anode and HTC-CC as current collector. The cell was firstly charged to 2.8 V followed by full discharge and charge in the range of 1-2.8 V, during which Li_2S_4 was stepwise oxidized to high-order polysulphides (Li_2S_n, $n \geq 8$) or elemental sulphur. In the meantime, Li^+ ions in pre-lithiated Al-Li alloy was extracted from the anode and reacted with Li_2S_4. Briefly speaking, CC and HTC-CC current collectors (described in the experimental section) were compared with the aim of studying Li_2S deposition, while Li metal was also investigated in terms of Li dendrite formation.

The electrochemical reversibility of cells Al-Li | CC and Al-Li | HTC-CC can be determined from Fig. 7b at 10^{th} cycle after cell stabilization. It is noted that the Al-Li | CC cell has higher polarization of 0.57 V than the 0.45 V voltage hysteresis of Al-Li | HTC-CC, showing the better sulphur activation and higher voltage efficiency when the HTC-CC was used as the cathode. The Al-Li | CC cell delivered low specific capacity of around 350 mA h g^{-1}, corresponding to 22 % sulphur utilization. In contrast, nearly 700 mA h g^{-1} sulphur capacity could be achieved for the Al-Li | HTC-CC cell, with two obvious plateaus between the range of 2.05 V – 2.1 V and 1.55 V – 1.6 V, which were attributed to the slightly higher potential (~0.3 V) of Al-Li alloy than Li metal (Fig. S8). The smaller polarization of HTC-CC than CC was ascribed to the uniform and thin layer coverage of Li_2S on HTC-CC that is beneficial for Li_2S re-activation upon charging. The Al-Li | HTC-CC cell also exhibited superior rate capability as shown in Fig. 7c. For example, a sulphur capacity of 250 mA h g^{-1} can be obtained at 2 C rate, showing a remarkably enhanced rate performance when compared with the Al-Li | CC cell.

The electrochemical impendence spectroscopy (EIS) was carried out in order to study the influence of cathode on cell resistance of Al-Li | CC and Al-Li | HTC-CC cells, namely Ohmic resistance (R_{ohm}), interfacial resistance (R_{inter}) and charge transfer resistance (R_{ct}). The high frequency area represents the Ohmic resistance of the cell, which is the intercept with the X axis. The mid-frequency is typically for the interfacial resistance between electrodes and catholyte during the polysulphide conversion, as determined by the diameter of the semi-

circle. The charge transfer resistance of the polysulphide ions in catholyte can be derived from the low-frequency part[46,47]. Fig. S12-S13 show that the evolution of the resistance values for both cells decreased after the 1st cycle, which can be attributed to the activation. First of all, the Ohmic impedance of Al-Li | CC is twofold higher than Al-Li | HTC-CC, demonstrating that the conductivity has been greatly enhanced with the more graphitic HTC-CC cathode. Secondly, the interfacial resistance of the Al-Li | HTC-CC cell (90 to 180 ohm) is approximately half of that with Al-Li | CC (180 to 300 ohm). The relatively low charge transfer resistance of Al-Li | HTC-CC might be resulted from the relatively smaller porosity in HTC-CC, as well as the enlarged external surface roughness[48]. The cyclic voltammogram (CVs) of Al-Li | CC and Al-Li | HTC-CC cells are shown in Fig. S14 (a, b). The first cycle which has lower cathodic peak and higher anodic peak is ascribed to the activation process[8,49], which is consistent with the EIS analysis. Further analysis of CV curve at different scan rates in Fig. S14 (c, d) shows the reaction is diffusion controlled[50].

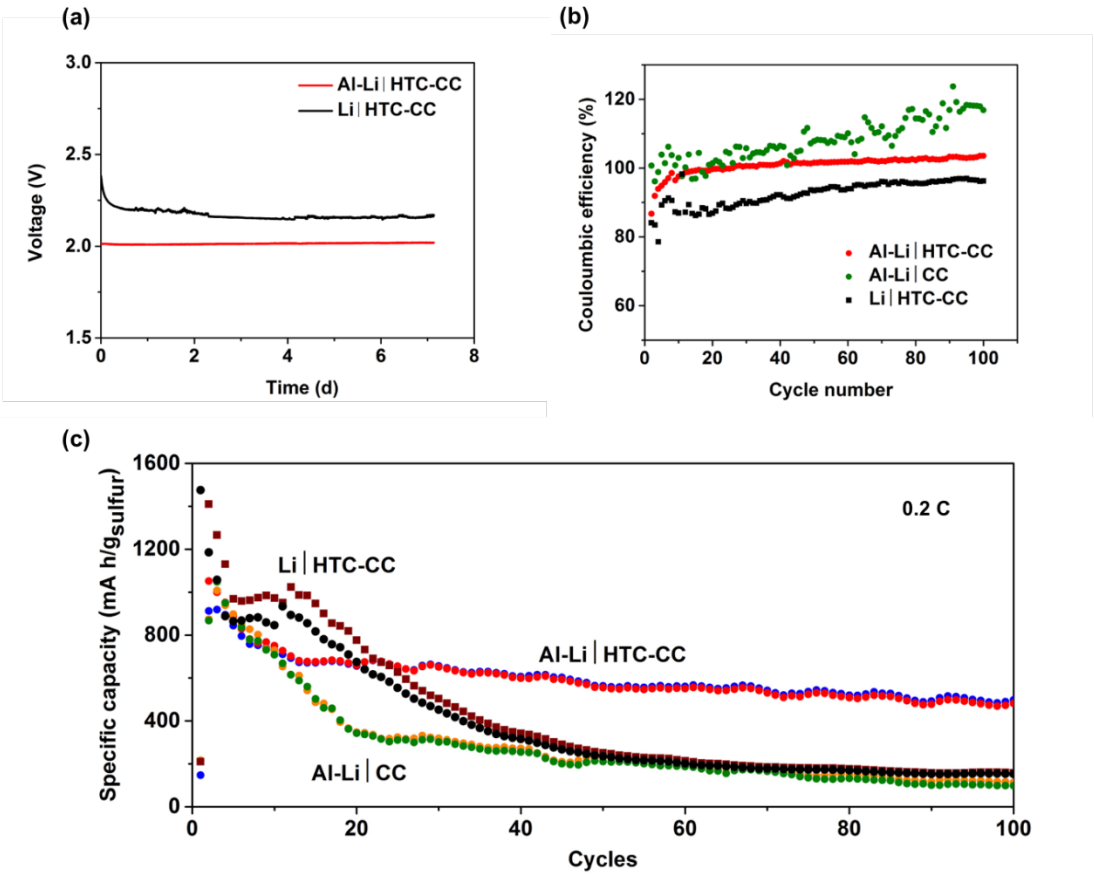

Fig. 8 Electrochemical performance of the Li-metal-free and $LiNO_3$-free Li-ion polysulfide cells. (a) Self-discharge test of Al-Li | HTC-CC and Li | HTC-CC full cell; (b) Coulombic efficiency and (c) Cycling stability of Al-Li | HTC-CC, Li | HTC-CC and Al-Li | CC full cells during 100 cycles.

The profiles for the self-discharge test of both Li | HTC-CC and Al-Li | HTC-CC cells are shown in Fig. 8a. For the Li | HTC-CC cell, the open circuit voltage (OCV) kept dropping after rest for 18 h, whereas the OCV of the Al-Li | HTC-CC cell kept steady at 2.05 V. After 18 h rest, the OCV trace of Li | HTC-CC cell stabilized, but still fluctuated indicative of the strong self-discharge behaviour. The rather stable OCV curve of Al-Li | HTC-CC full cell in 7 days was noticeable. Fig. 8b compares the coulombic efficiency (CE) for three cells, namely Li | HTC-CC, Al-Li | HTC-CC and Al-Li | CC. With the cycle number increased, the CE curve of Al-Li | CC indicated an upward tendency, which is over 100%. It is because of the shuttling phenomenon where lithium polysulphides dissolved and shuttled in the electrolyte, leading to low sulphur utilization and capacity. While for the Al-Li | HTC-CC, it had the best CE that close to 100 %. Li | HTC-CC cell had low CE of 82 % at the beginning and later increased gradually to 92 %, which is the indication of incomplete sulphur utilization when charging back to elemental sulphur state. As exhibited in Fig. 8c, the specific capacity based on sulphur content for the Al-Li | HTC-CC cell retained 500 mA h g^{-1} at the 100^{th} cycle with a retention of 74%. The sharp capacity decrease within the beginning cycles could be the activation process[51]. The Al-Li alloy anode could compensate Li ions with 90 – 92 % coulombic efficiency during the alloying/de-alloying process (Fig. S6). The stability of Al-Li | CC cell is poor with only 50 mA h g^{-1} capacity after 100 cycles. The Li | HTC-CC cell also showed poor stability. This further illustrates that the Al-Li alloy anode is more advantageous to the cell stability in terms of $LiNO_3$-free condition. Furthermore, compared with the Al-Li | HTC-CC cell, the Al-Li | CC cell exhibited slow kinetics, poor stability and low capacity. Pan et al.[19] revealed that the strong substrate-polysulphides interaction could passivate the sulphides deposition, giving rise to the enlarged overpotential and poor cyclic stability. The fast kinetics and good stability of lithium polysulphides on HTC-CC could be correlated with the HTC coating which concealed the stronger polar Al_2O_3 species. The mild content of oxygen (at 3.5 %) in the annealed HTC layer acts as soft mediator to balance the adsorption and desorption of sulphides species. The strong binding between Al_2O_3 and lithium sulphides is responsible for the retarded charge transfer and the poor cyclic stability[15]. However, the capacity loss of the Al-Li/HTC-CC LiPS full cell is likely related to the 90 – 92 % coulombic efficiency of alloy, which usually leads to gradual capacity loss especially for long cycles. On the other hand, the use of low-porosity open-network carbon cloth as cathode is another plausible factor.

Conclusion

We demonstrate the improved performance of a Li-ion polysulphide full cell with hydrothermal carbon@carbon cloth (HTC-CC) cathode and Al-Li alloy anode. By employing a new parallel interface engineering (PIE) strategy, we show that the better cell voltage efficiency, higher sulphur utilization, suppressed anode dendrite growth are achievable in the Li-metal-free $LiNO_3$-free conditions. It is noticeable that the surface chemical homogeneity of the carbon current collector dominates the uniform film-like morphology of Li_2S deposition, and hence largely improves the cell efficiency. Meanwhile, the use of Al-Li alloy with an implanted SEI coating can effectively protect the anode from the side reactions with polysulphide as well as the growth of lithium dendrite due to the unfavourable potential region. Overall, this PIE approach demonstrates a new concept for the full cell design via the synchronous mitigation of the troublesome processes at anode and cathode via interface modifications.

Acknowledgements

This work is financially supported by the Australian Research Council Discovery Project (DP160103244), and the UNSW-THU seed grant. J. L. acknowledges the CSC funds. N. S. acknowledges the Australian Research Council DECRA Project (DE160100237). Part of this research was undertaken on the Powder Diffraction beamline at the Australian Synchrotron, part of ANSTO. The authors acknowledge the facilities and the scientific and technical assistance from Mark Wainwright Analytical Centre and at the Electron Microscope Unit at UNSW.

Conflicts of interest

There are no conflicts of interest to declare.

Reference

1 M.-K. Song, E. J. Cairns and Y. Zhang, *Nanoscale*, 2013, **5**, 2186–204.
2 J. Brückner, S. Thieme, F. Böttger-Hiller, I. Bauer, H. T. Grossmann, P. Strubel, H. Althues, S. Spange and S. Kaskel, *Adv. Funct. Mater.*, 2014, **24**, 1284–1289.
3 J. Hassoun and B. Scrosati, *Angew. Chemie Int. Ed.*, 2010, **49**, 2371–2374.
4 R. Elazari, G. Salitra, G. Gershinsky, A. Garsuch, A. Panchenko and D. Aurbach, *Electrochem. commun.*, 2012, **14**, 21–24.
5 Z. Wei Seh, W. Li, J. J. Cha, G. Zheng, Y. Yang, M. T. McDowell, P.-C. Hsu and Y.

Cui, *Nat. Commun.*, 2013, **4**, 1331.
6 B. Zhang, Y. Zhao, J. Liu, X. Wang, D. Li and X. Li, *Electrochim. Acta*, 2017, **248**, 416–424.
7 J. Song, T. Xu, M. L. Gordin, P. Zhu, D. Lv, Y. B. Jiang, Y. Chen, Y. Duan and D. Wang, *Adv. Funct. Mater.*, 2014, **24**, 1243–1250.
8 L. Wang, Z. Yang, H. Nie, C. Gu, W. Hua, X. Xu, X. Chen, Y. Chen and S. Huang, *J. Mater. Chem. A*, 2016, **4**, 15343–15352.
9 G. Zhou, E. Paek, G. S. Hwang and A. Manthiram, *Nat. Commun.*, 2015, **6**, 7760.
10 J. Zhang, Y. Shi, Y. Ding, L. Peng, W. Zhang and G. Yu, *Adv. Energy Mater.*, 2017, 1–7.
11 D. Liu, C. Zhang, G. Zhou, W. Lv, G. Ling, L. Zhi and Q. H. Yang, *Adv. Sci.*, 2018, **5**, 1700270–1700282.
12 T. Zhou, W. Lv, J. Li, G. Zhou, Y. Zhao, S. Fan, B. Liu, B. Li, F. Kang and Q.-H. Yang, *Energy Environ. Sci.*, 2017, **10**, 1694–1703.
13 Z. Sun, J. Zhang, L. Yin, G. Hu, R. Fang, H.-M. Cheng and F. Li, *Nat. Commun.*, 2017, **8**, 14627.
14 W. Bao, D. Su, W. Zhang, X. Guo and G. Wang, *Adv. Funct. Mater.*, 2016, **26**, 8746–8756.
15 X. Tao, J. Wan, C. Liu, H. Wang, H. Yao, G. Zheng, Z. W. Seh, Q. Cai, W. Li, G. Zhou, C. Zu and Y. Cui, *Nat. Commun.*, 2016, **7**, 1–9.
16 Y. Fu, Y. S. Su and A. Manthiram, *Angew. Chemie - Int. Ed.*, 2013, **52**, 6930–6935.
17 Y. Yang, G. Zheng and Y. Cui, *Energy Environ. Sci.*, 2013, **6**, 1552–1558.
18 L. Qie, C. Zu and A. Manthiram, *Adv. Energy Mater.*, 2016, **6**, 1–7.
19 H. Pan, J. Chen, R. Cao, V. Murugesan, N. N. Rajput, K. S. Han, K. Persson, L. Estevez, M. H. Engelhard, J. G. Zhang, K. T. Mueller, Y. Cui, Y. Shao and J. Liu, *Nat. Energy*, 2017, **2**, 813–820.
20 F. Y. Fan, W. C. Carter and Y.-M. Chiang, *Adv. Mater.*, 2015, **27**, 5203–5209.
21 J. Guo, X. Du, X. Zhang, F. Zhang and J. Liu, *Adv. Mater.*, 2017, **1700273**, 1700273.
22 A. Rosenman, R. Elazari, G. Salitra, E. Markevich, D. Aurbach and A. Garsuch, *J. Electrochem. Soc.*, 2015, **162**, A470–A473.
23 S. S. Zhang, *J. Electrochem. Soc.*, 2012, **159**, A920–A923.
24 M. N. Obrovac and V. L. Chevrier, *Chem. Rev.*, 2014, **114**, 11444–11502.
25 M. M. Nicholson, *J. Electrochem. Soc.*, 1974, **121**, 734–738.
26 D. Lin, Y. Liu, Z. Liang, H.-W. Lee, J. Sun, H. Wang, K. Yan, J. Xie and Y. Cui, *Nat. Nanotechnol.*, 2016, **11**, 626–632.
27 J. Sun, Q. (Ray) Zeng, R. Lv, W. Lv, Q.-H. Yang, R. Amal and D.-W. Wang, *Energy Storage Mater.*, 2018, **15**, 209–217.
28 J. C. Pramudita, S. Schmid, T. Godfrey, T. Whittle, M. Alam, T. Hanley, H. E. A. Brand and N. Sharma, *Phys. Chem. Chem. Phys.*, 2014, **16**, 24178–24187.
29 P. Serras, V. Palomares, T. Rojo, H. E. A. Brand and N. Sharma, *J. Mater. Chem. A*, 2014, **2**, 7766–7779.
30 S. Kitagawa, R. Kitaura and S. Noro, *Angew. Chemie Int. Ed.*, 2004, **43**, 2334–2375.
31 C. D. Wagner, D. E. Passoja, H. F. Hillery, T. G. Kinisky, H. A. Six, W. T. Jansen and J. A. Taylor, *J. Vac. Sci. Technol.*, 1982, **21**, 933–944.
32 R. Zhang, X. R. Chen, X. Chen, X. B. Cheng, X. Q. Zhang, C. Yan and Q. Zhang, *Angew. Chemie - Int. Ed.*, 2017, **56**, 7764–7768.
33 T. Ko and C. Chen, *J. Appl. Polym. Sci.*, 1998, **71**, 2219–2225.
34 J. Robertson, *Adv. Phys.*, 1986, **35**, 317–374.
35 F. Tuinstra and J. L. Koenig, *J. Chem. Phys.*, 1970, **53**, 1126–1130.
36 X. B. Cheng, C. Yan, J. Q. Huang, P. Li, L. Zhu, L. Zhao, Y. Zhang, W. Zhu, S. T.

Yang and Q. Zhang, *Energy Storage Mater.*, 2017, **6**, 18–25.
37 H. Ota, Y. Sakata, A. Inoue and S. Yamaguchi, *J. Electrochem. Soc.*, 2004, **151**, A1659.
38 K. Edström, M. Herstedt and D. P. Abraham, *J. Power Sources*, 2006, **153**, 380–384.
39 M. Herstedt, H. Rensmo, H. Siegbahn and K. Edström, *Electrochim. Acta*, 2004, **49**, 2351–2359.
40 M. Herstedt, D. P. Abraham, J. B. Kerr and K. Edström, *Electrochim. Acta*, 2004, **49**, 5097–5110.
41 Z. Peng, N. Zhao, Z. Zhang, H. Wan, H. Lin, M. Liu, C. Shen, H. He, X. Guo, J. G. Zhang and D. Wang, *Nano Energy*, 2017, **39**, 662–672.
42 E. Markevich, G. Salitra, F. Chesneau, M. Schmidt and D. Aurbach, *ACS Energy Lett.*, 2017, **2**, 1321–1326.
43 X. Q. Zhang, X. B. Cheng, X. Chen, C. Yan and Q. Zhang, *Adv. Funct. Mater.*, 2017, **27**, 1605989–1605997.
44 G. Wollensak, E. Spoerl and T. Seiler, *Am. J. Ophthalmol.*, 2003, **135**, 620–627.
45 X. B. Cheng, C. Yan, X. Chen, C. Guan, J. Q. Huang, H. J. Peng, R. Zhang, S. T. Yang and Q. Zhang, *Chem*, 2017, **2**, 258–270.
46 F. Y. Fan, W. H. Woodford, Z. Li, N. Baram, K. C. Smith, A. Helal, G. H. Mckinley, W. C. Carter and Y. Chiang, *Nano Lett.*, 2014, **14**, 2210–2218.
47 G. Zhou, L. Li, D. W. Wang, X. Y. Shan, S. Pei, F. Li and H. M. Cheng, *Adv. Mater.*, 2015, **27**, 641–647.
48 H. Chen, Q. Zou, Z. Liang, H. Liu, Q. Li and Y.-C. Lu, *Nat. Commun.*, 2015, **6**, 5877.
49 Z. Xiao, Z. Yang, H. Nie, Y. Lu, K. Yang and S. Huang, *J. Mater. Chem. A*, 2014, **2**, 8683–8689.
50 M. V. Mirkin, A. J. Bard and L. O. S. Bulhões, *J. Am. Chem. Soc.*, 1993, **115**, 201–204.
51 G. C. Li, G. R. Li, S. H. Ye and X. P. Gao, *Adv. Energy Mater.*, 2012, **2**, 1238–1245.